

DETAILS OF TURBULENCE MODELING IN NUMERICAL SIMULATIONS OF SCRAMJET INTAKE

T. Nguyen* , G. Schieffer* , C. Fischer** , H. Olivier** , M. Behr* and B. Reinartz*

*Chair for Computational Analysis of Technical Systems, Center for Computational Engineering Science

**Shock Wave Laboratory

RWTH Aachen University, 52056 Aachen, Germany

Keywords: *turbulence modeling, hypersonic, scramjet intake, compressibility correction*

Abstract

This paper presents a combined study of simulation and experiment of hypersonic intake flow. A finite-volume flow solver is used to simulate a scramjet intake configuration and the results are compared against the measurements. Turbulence closure is achieved using two eddy-viscosity models and a differential Reynolds-stress model. In order to improve the prediction of the simulation, we consider the need to include the direct contribution of turbulence kinetic energy into the formulation of total energy and the Boussinesq hypothesis for the eddy-viscosity turbulence models in the numerical simulations of hypersonic flows. In addition we also model the turbulent diffusion in the energy equation and the dilatation dissipation in the length-scale equation of the turbulence model and assess the effects of these terms. It is shown that the turbulence kinetic energy should not be neglected in the formulation of the total energy and the compressibility corrections may provide some improvements. 3D effects and numerical issues such as stability and grid convergence are discussed.

Nomenclature

$(.)^{(t)}$ = turbulent variables

$(.)_w$	= wall variables
ρ	= density
U_k	= velocity component
u_k''	= velocity fluctuation component
p	= pressure
T	= temperature
τ_{ij}	= shear stress component
E	= total energy
H	= total enthalpy
e	= internal energy
h	= internal enthalpy
q_k	= heat flux component
D_{kk}	= turbulent diffusion
C_v	= specific heat at constant volume
C_p	= specific heat at constant pressure
k	= turbulence kinetic energy
ω	= specific dissipation rate
R_{ij}	= Reynolds-stress component
R	= specific gas constant
γ	= ratio of specific heats
μ	= viscosity
δ_{ij}	= Kronecker delta
S_{ij}^*	= traceless strain rate tensor
λ	= heat conductivity
Pr	= Prandtl number
M_T	= turbulence Mach number
a	= speed of sound

1 Introduction

This work is a part of an on going research on supersonic combustion ramjet (scramjet) engines in Germany [15]. A scramjet intake consists of several external compression ramps and an interior part. The flow is compressed through a series of oblique shock waves generated by the ramp and the cowl in which multiple interesting physical phenomena may occur, such as rapid compression/expansion, shock-boundary layer interaction, etc. (see Fig. 1). These phenomena may trigger some other complex processes, e.g., laminar-turbulent transition, compressible relaminarization, flow separation, etc. In this paper, we use QUADFLOW, a well-validated cell-centered finite volume flow solver [2], to simulate the flow inside a scramjet intake model that was built and tested at the Shock Wave Laboratory [5].

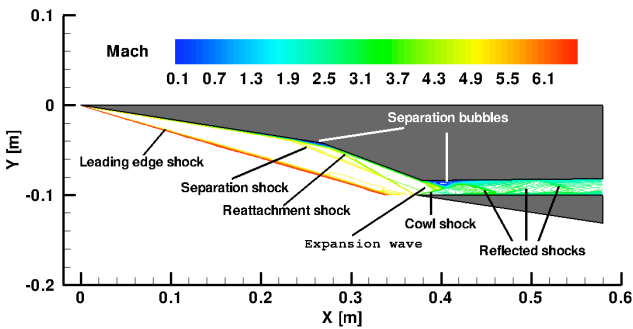


Fig. 1 : Typical configuration of a Scramjet intake and the associated flow features. The flow is from left to right. The free-stream Mach number and the unit Reynolds number are 6.7 and $3.8 \times 10^6 \text{ m}^{-1}$, respectively.

Numerical simulations of hypersonic flows require additional closure approximations for compressibility effects. This is because not only the density is now varying but there are also additional correlations due to the fluctuating density. Furthermore, since the velocity is several order of magnitude larger than in incompressible flow, the magnitudes of velocity fluctuations and turbulence kinetic energy are also larger. In order to take into account these effects properly, we implement and analyze the following modi-

fications in QUADFLOW: the inclusion of turbulence kinetic energy to the total energy, the use of full Boussinesq approximation (in which turbulence kinetic energy is included), the importance of turbulent diffusion in the energy equation, and the effects of Zeman/ Wilcox compressibility corrections using dilatation dissipation [12]. These modifications for compressible flows were suggested by several researchers, e.g., Wilcox [16], Rumsey [12].

2 Experiment

The scramjet intake used for simulation in this work was designed under the Research Training Group GRK 1095 "Aero-Thermodynamic Design of a Scramjet Propulsion System for Future Space Transportation Systems" in Germany [15]. The intake is 580 mm long and 100 mm wide and comprises of two external compression ramps and an interior part. The first ramp and the second ramp are inclined to the horizontal surface by 9° and 20.5° , respectively. The leading edges of the first ramp and the cowl lip are sharp. The second ramp and the interior part is connected by a sharp expansion corner. Schematic drawing of the intake is shown in Fig. 2.

The model was tested in the hypersonic shock tunnel TH2 in helium-driven mode at the Shock Wave Laboratory, RWTH Aachen University. The tunnel can simulate re-entry flow conditions with total enthalpies from 1.5 to 14.6 MJ/kg and Mach numbers from 6.6 to 14 using helium-driven or detonation-driven mode. The exact dimensions of the intake, detailed measurement techniques and experimental results can be found in Neuenhahn and Olivier [10] and Fischer and Olivier [5].

Two inflow conditions were used in the experiments and are listed in Table 1. Condition A was used for the measurements of pressure and heat transfer on the external ramps and condition B was used for the measurements in the interior part. In the experiment, pressure and heat transfer rate (Stanton number) were measured by Kulite pressure probes and thermocouples, respectively [5]. In the numerical simulations, only condition

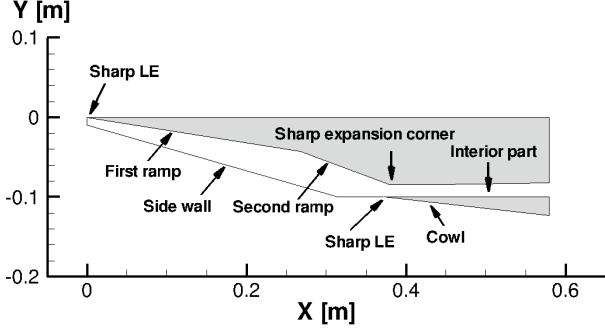


Fig. 2 : Schematic drawing of the SWL intake.

A was used as the free-stream condition and the reference state in the analysis of the results.

Cond.	M_∞ [-]	$Re_{\infty,m}$ [1/m]	T_0 [K]	T_∞ [K]	T_w [K]
A	6.7	3.8×10^6	1300	129	300
B	7.7	4.1×10^6	1520	125	300

Table 1: Inflow and boundary conditions in the experiments.

3 Physical Modeling

We consider a set of equations representing mass, momentum and energy conservation within the framework of Reynolds-averaged Navier Stokes (RANS) computation:

$$\frac{\partial \bar{\rho}}{\partial t} + \frac{\partial}{\partial x_k} (\bar{\rho} \tilde{U}_k) = 0, \quad (1)$$

$$\frac{\partial (\bar{\rho} \tilde{U}_i)}{\partial t} + \frac{\partial}{\partial x_k} (\bar{\rho} \tilde{U}_i \tilde{U}_k + \bar{\rho} \widetilde{u_i'' u_k''}) = -\frac{\partial \bar{p}}{\partial x_i} + \frac{\partial \bar{\tau}_{ik}}{\partial x_k}, \quad (2)$$

$$\begin{aligned} \frac{\partial (\bar{\rho} \tilde{E})}{\partial t} + \frac{\partial}{\partial x_k} (\bar{\rho} \tilde{H} \tilde{U}_k + \bar{\rho} \widetilde{u_i'' u_k'' \tilde{U}_i}) = \\ \frac{\partial}{\partial x_k} (\bar{\tau}_{ik} \tilde{U}_i) - \frac{\partial}{\partial x_k} (\bar{q}_k + \bar{q}_k^{(t)}) + \bar{\rho} D_{kk}. \end{aligned} \quad (3)$$

The total energy and the total enthalpy are:

$$\tilde{E} = \tilde{e} + \tilde{U}_k \tilde{U}_k / 2 + \tilde{k}; \quad \tilde{e} = C_v \tilde{T}, \quad (4)$$

$$\tilde{H} = \tilde{h} + \tilde{U}_k \tilde{U}_k / 2 + \tilde{k}; \quad \tilde{h} = C_p \tilde{T}. \quad (5)$$

In these equations the overbar ($\bar{\phi}$) and the tilde ($\tilde{\phi}$) denote ensemble and mass-weighted averages, respectively. The velocity fluctuation correlation in Eqn. 2 and Eqn. 3 is denoted as $\bar{\rho} \widetilde{u_i'' u_k''} = \bar{\rho} \tilde{R}_{ij}$. The contribution of turbulence kinetic energy to the total energy and total enthalpy in Eqn. 4 and Eqn. 5 are normally omitted in simulating subsonic and supersonic flows. Here we will consider the importance of this addition. With the inclusion of the turbulence kinetic energy, the pressure is then computed as follows:

$$\bar{p} = \bar{\rho} R \tilde{T} = (\gamma - 1) \bar{\rho} \tilde{e} = (\gamma - 1) \bar{\rho} (\tilde{E} - \tilde{U}_k \tilde{U}_k / 2 - \tilde{k}). \quad (6)$$

The turbulent diffusion ($\bar{\rho} D_{kk}$) in Eqn. 3 is modeled based on simple gradient diffusion hypothesis for eddy-viscosity models [16]:

$$\bar{\rho} D_{kk} = \frac{\partial}{\partial x_k} \left[\left(\bar{\mu} + \sigma^* \bar{\mu}^{(t)} \right) \frac{\partial \tilde{k}}{\partial x_k} \right], \quad (7)$$

and generalized gradient diffusion hypothesis for Reynolds stress model [4]:

$$\bar{\rho} D_{ij} = \frac{\partial}{\partial x_k} \left[\left(\bar{\mu} \delta_{kl} + \sigma^* \frac{\bar{\rho}}{\omega} \tilde{R}_{kl} \right) \frac{\partial \tilde{R}_{ij}}{\partial x_l} \right]. \quad (8)$$

σ^* is a coefficient in the model and is set to 0.5 in this context. We will also assess the effect of this term on the numerical results.

We assume that gas is ideal ($\bar{p} = \bar{\rho} R \tilde{T}$) and calorically perfect (C_p and C_v are constants) and fluid is Newtonian so that the laminar stress tensor can be given as:

$$\bar{\tau}_{ij} = 2\bar{\mu} \tilde{S}_{ij}^*; \quad \tilde{S}_{ij}^* = \frac{1}{2} \left(\frac{\partial \tilde{U}_i}{\partial x_j} + \frac{\partial \tilde{U}_j}{\partial x_i} - \frac{2}{3} \frac{\partial \tilde{U}_k}{\partial x_k} \delta_{ij} \right). \quad (9)$$

In Eqn. 9, the laminar dynamic viscosity is computed using Sutherland's formula. The laminar and turbulent heat fluxes in Eqn. 3 are modeled based on Fourier type heat conduction:

$$\bar{q}_i = -\bar{\lambda} \frac{\partial \tilde{T}}{\partial x_i}; \bar{q}_i^{(t)} = \bar{\rho} \tilde{h} u_k'' = -\bar{\lambda}^{(t)} \frac{\partial \tilde{T}}{\partial x_i}, \quad (10)$$

in which the laminar/turbulent heat conductivity is computed via the laminar/turbulent viscosity and a constant laminar/turbulent Prandtl number:

$$\bar{\lambda} = \frac{C_p \bar{\mu}}{Pr}; \bar{\lambda}^{(t)} = \frac{C_p \bar{\mu}^{(t)}}{Pr_t}. \quad (11)$$

$\bar{\mu}^{(t)}$ is determined by an eddy-viscosity model scheme for both eddy-viscosity models and Reynolds-stress model.

Regarding the turbulence closure for $\bar{\rho} \tilde{R}_{ij}$, we focus on three turbulence models: Menter's shear stress transport (SST) model [8], Menter's γ - Re_θ transition model (SST transition) [9], [7] and Eisfeld's SSG/LRR- ω Reynolds stress model (RSM) [4], [1].

In the SST model the turbulence kinetic energy \tilde{k} and the specific dissipation rate ω are solved by two transport equations in addition to the system of Eqn. 1 - 3:

$$\frac{\partial (\bar{\rho} \tilde{k})}{\partial t} + \tilde{U}_k \frac{\partial (\bar{\rho} \tilde{k})}{\partial x_k} = P_k - \beta^* \rho k \omega + \bar{\rho} D_k, \quad (12)$$

$$\frac{\partial (\bar{\rho} \omega)}{\partial t} + \tilde{U}_k \frac{\partial (\bar{\rho} \omega)}{\partial x_k} = P_\omega - \beta \rho \omega^2 + \bar{\rho} D_\omega + \bar{\rho} CD_\omega, \quad (13)$$

P, D and CD denote production term, diffusion term and cross-diffusion term, respectively. The detailed formulations of these terms are given in Menter [8]. In this context, we only modify β and β^* using the compressibility corrections discussed later. The eddy-viscosity is then determined as a function of \tilde{k} and ω [8]. The Reynolds stresses are defined using Boussinesq approximation:

$$\bar{\rho} \tilde{R}_{ij} = -2\mu^{(t)} \tilde{S}_{ij}^* + \frac{2}{3} \bar{\rho} \tilde{k} \delta_{ij}. \quad (14)$$

The last term on the right hand side, which ensures that the trace of the Reynolds stress tensor is $2\tilde{k}$, is also normally neglected in numerical simulations of low-speed flows and its importance will be assessed in this paper.

Menter's γ - Re_θ transition model is based on two transport equations for the intermittency γ and the momentum thickness Reynolds number Re_θ . The physics of the transition process is not modeled by the transport equations but entirely contained in a set of experimental correlation. Details of the implementation of this model into QUADFLOW and its validation are given in Krause et al. [7].

In the SSG/LRR- ω Reynolds stress model, transport equations of the Reynolds stresses are solved. Even though this makes the computations more expensive, the model does not suffer from the limitation of the Boussinesq approximation (Eqn. 14) and naturally includes the effects of streamline curvature, sudden changes in strain rates, secondary motion etc. Menter's blending function [8] is used in the SSG/LRR- ω model so that the model behaves like the LRR model [11] in the near wall region and the SSG model [13] in the far field. Details of the implementation of this model into QUADFLOW can be found in Bosco et al [1].

In this paper, we consider two compressibility corrections due to dilatation dissipation proposed by Zeman and Wilcox [12] for the SST turbulence model. The main idea of these corrections is that the turbulence dissipation can be split into two parts, namely, solenoidal dissipation and dilatation dissipation. The latter is only important in high Mach number flows in which the turbulence Mach number is considerable large. These corrections were developed for boundary layer flows and require changes in the coefficients of the dissipation terms in the transport equations for \tilde{k} and ω as follows:

$$\beta_c^* = \beta^* [1 + \zeta^* F(M_T)], \quad (15)$$

$$\beta_c = \beta - \beta^* \zeta^* F(M_T), \quad (16)$$

where $M_T = (\sqrt{2\tilde{k}})/a$ is the turbulence Mach number and a is the local speed of sound. In the Zeman version, $F(M_T)$ is:

$$F(M_T) = \left[1 - \exp \left(- \left(\frac{M_T - M_{T_0}}{\Lambda} \right)^2 \right) \right] H(M_T - M_{T_0}), \quad (17)$$

with $\zeta^* = 0.75$, $M_{T_0} = 0.2$, $\Lambda = 0.6$, and H is the Heaviside function.

In the Wilcox correction, $F(M_T)$ is:

$$F(M_T) = (M_T^2 - M_{T_0}^2) H(M_T - M_{T_0}), \quad (18)$$

with $\zeta^* = 2$ and $M_{T_0} = 0.25$.

4 Numerical Method

We perform the computations using QUADFLOW, which solves the RANS equations in 2D and 3D. The spatial discretization of the governing equations is based on a cell-centered finite volume flow scheme suited for unstructured grids. In this study, an AUSMDV upwind method is used to discretize the convective fluxes and second-order accuracy is achieved by a linear reconstruction. The viscous fluxes are discretized by quasi-central differencing. The mean flow equations are integrated in time by a fully implicit Newton-Krylov method or an explicit five-stage Runge-Kutta scheme.

We simulate a test case in which the following boundary conditions are used: supersonic inflow, supersonic outflow and solid wall. At supersonic inflow boundaries, the values are prescribed using the experimental data. The free-stream turbulence intensity was fixed at 0.5 %. At supersonic outflow boundaries, the variables are extrapolated from the interior assuming zero-gradient. At solid walls, the no-slip condition is enforced and isothermal condition is used. The turbulence kinetic energy and the Reynolds stresses are set to zero at the wall and the respective lengthscale is prescribed based on the first grid spacing according to Menter [8]:

$$\omega_w = C_M \frac{6\mu_w}{\rho_w \beta_1 d_1^2}. \quad (19)$$

Here C_M and β_1 are constants and have been set to 10 and 0.075, respectively, and d_1 is the distance to the cell center next to the wall.

5 Grid Convergence Study

The grid used in this work was originally created by Krause and Ballmann [6] using a multi-block elliptic structured grid generator (MegaCads [3]). The grid points in the wall normal direction are stretched by Poisson distribution in order to achieve y^+ smaller than 1 close to the wall everywhere in the computational domain (the minimum distance to the wall is at least 10^{-6} meter). The transverse grid lines were created in such a way that they are almost always perpendicular to the wall surface (Fig. 3).

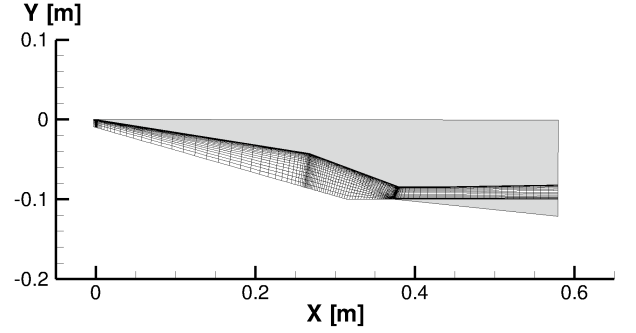


Fig. 3 : Grid distribution in the symmetry plane of the SWL intake. Every fourth grid line of the coarse grid is shown.

Three different grids were used in 2D computations: a coarse grid (50000 cells), a medium grid (200000 cells) and a fine grid (800000 cells). In 3D computations, the 2D coarse grid is extended in the spanwise direction for half of the width of the intake and results in a 3D grid of approximately 3 million cells. The grid lines in the spanwise direction are also clustered towards the sidewall (Fig. 4).

Grid convergence study was performed for the 2D computations using the three grids mentioned above in which the resolution from one grid to another was refined by doubling the number of cells in both the streamwise and wall normal directions. The computations were done us-

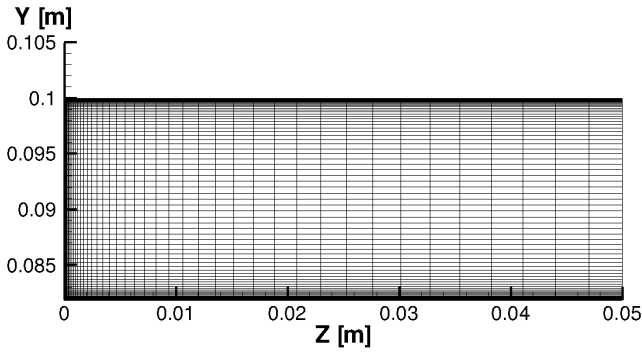


Fig. 4 : Grid distribution at the exit plane of the 3D grid for the SWL intake.

ing the original SST model without any modifications mentioned in the previous section. Fig. 5 and Fig. 6 show the wall pressure distribution and the Stanton number along the ramps and the upper wall of the interior part for the three grids. It can be seen that there are still small differences in the results predicted by the medium grid and the fine grid. However, due to resource constraint, the medium grid was used for all the 2D computations of the intake in the subsequent sections unless otherwise stated.

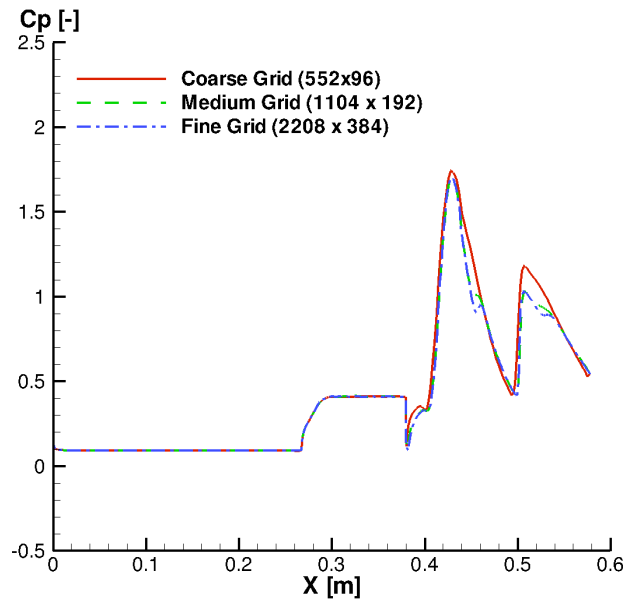


Fig. 5 : Grid sensitivity analysis: pressure along the upper wall of the symmetry plane, SST turbulence model.

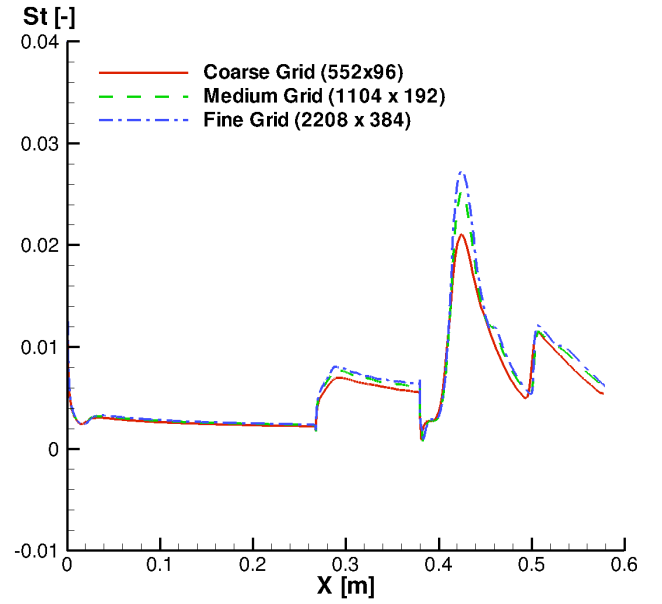


Fig. 6 : Grid sensitivity analysis: Stanton number along the upper wall of the symmetry plane, SST turbulence model.

6 Results

We use the following terminologies in the legend of the results to distinguish the different modifications considered in this work:

- Original: the original formulation for low-speed flows.
- k inclusion: inclusion of turbulence kinetic energy to the total energy (Eqn. 4 and Eqn. 5).
- Re tensor trace: the last term on the right hand side in Eqn. 14 is included. This is only applicable to the SST model.
- diffusion: the model of turbulent diffusion in the energy equation is used (Eqn. 7 and Eqn. 8). It should be noted that, for the RSM model, this term was modeled in the original implementation (see Bosco et al. [1]). We only consider the effect of this term in this work.
- ZemanCC: Zeman compressibility correction (Eqn. 15, Eqn. 16 and Eqn. 17).

- WilcoxCC: Wilcox compressibility correction (Eqn. 15, Eqn. 16 and Eqn. 18).

6.1 General Flow Features in Scramjet Intake

Fig. 1 illustrates the general flow features inside a scramjet intake. The flow is first compressed through an oblique shock wave from the leading edge of the first ramp. The pressure gradient due to the flow deflection between the first ramp and the second ramp is strong enough to cause a flow separation at the compression corner and the flow is also transitional from laminar to turbulent state over this separation bubble [7]. Prior to the entrance of the interior part, the flow experiences a supersonic expansion at the end of the second ramp. Compressible relaminarization may occur here in which the turbulence intensity decreases significantly and the velocity exhibits a laminar-like profile (but the boundary layer is not completely laminar). After expanding, the flow encounters an oblique shock wave from the cow lip. The large adverse pressure gradient produced by this shock wave boundary layer interaction causes a second separation bubble on the intake wall. Before this separation can be accurately predicted, the state of the boundary layer entering the interior part, which is a compressible turbulent flow over the expansion corner, must be known. Downstream of this bubble, the flow is going through several reflected shock waves and expansion waves before entering the combustion chamber.

Fig. 7 and Fig. 8 show the typical pressure and heat transfer distributions along the upper wall of the intake. For clarification, the geometry of the upper part of the intake is also shown in these figures (the scaling is not exact for better visualization). At the compression corner, the first separation bubble, over which the flow is transitional from laminar to turbulent, can be seen through a pressure plateau and a drop in Stanton number. After the reattachment shock wave, both the pressure and Stanton number rise steeply before leveling off on the second ramp. At the sharp convex corner, the pressure drops due to supersonic expansion and the Stanton number is also

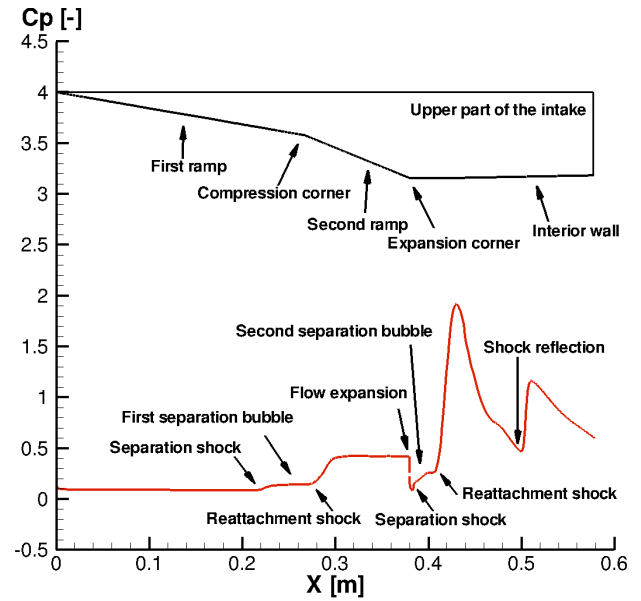


Fig. 7 : An example of pressure distribution along the upper wall of the symmetry plane of the intake. 2D simulation using the SST transition model.

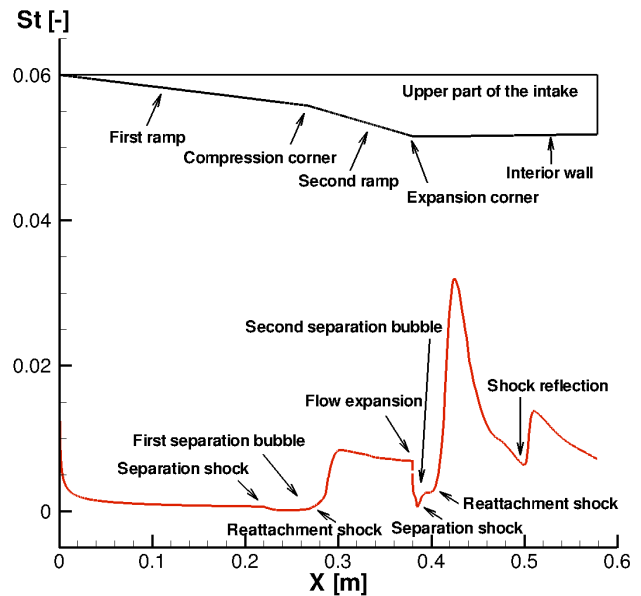


Fig. 8 : An example of the Stanton number distribution along the upper wall of the symmetry plane of the intake. 2D simulation using the SST transition model.

decreased which is an indication of compressible relaminarization. Inside the interior part, the

second separation bubble is formed due to the shock wave from the cowl lip and this can be seen through the plateaus in both pressure and Stanton number. Further downstream, reflected shock waves and expansion waves cause small jumps in pressure and heat transfer rate.

6.2 The Significance of Turbulence Kinetic Energy

We first assess the significance of the turbulence kinetic energy k in the scramjet intake by examining a 2D computation without k inclusion using the SST model. Fig. 9 shows the turbulence kinetic energy as a fraction of the total enthalpy. It can be seen that the magnitude of this ratio is about 0.05 to 0.1 across the separation bubble at the entrance of the interior part. The amplification of turbulence kinetic energy here is probably a result of the combined effects of adverse pressure gradient, concave streamline curvature, bulk compression and flow separation [14]. Furthermore, the amplification effect is more profound when the value of the density is combined with k as shown in Fig. 10 in which the multiplication of turbulence kinetic energy and density is plotted as a fraction of pressure. The magnitude of $\rho k/P$ is about 0.3 to 0.6 around the second separation bubble. The ratio is most significant in the reattachment region. This indicates that inclusion of turbulence kinetic energy will strongly influence the pressure (see Eqn. 6). From this observation, it can be concluded that inclusion of turbulence kinetic energy to the total energy is necessary in order to ensure exact conservation of energy and more accurate computation of pressure.

The qualitative effect of including k into the total energy is demonstrated in Fig. 11 and Fig. 12. The figures show the Mach lines at the entrance of the interior part, where the turbulence kinetic energy is significant (see Fig. 10), for two computations: one computation without k inclusion and another one with k inclusion. It can be seen that, with k inclusion, the onset of the second separation bubble is delayed and the separation bubble is also smaller. The differences appear most noticeably in the area where the turbu-

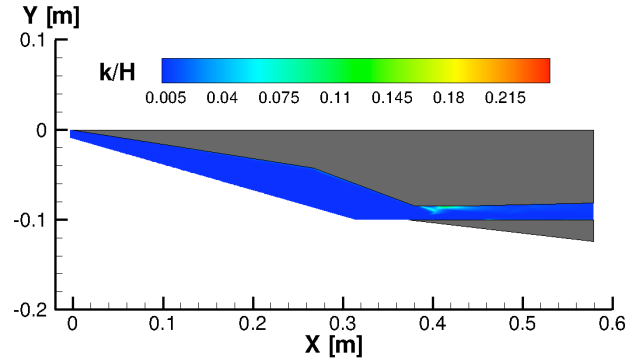


Fig. 9 : Contour plot of turbulence kinetic energy as fraction of total enthalpy. 2D simulation of the intake using the SST model.

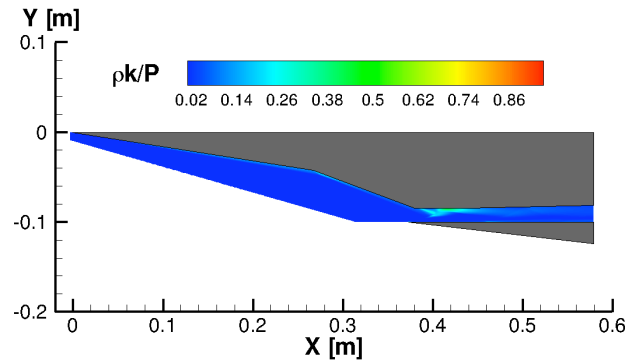


Fig. 10 : Contour plot of turbulence kinetic energy (multiplied by density) as fraction of pressure. 2D simulation of the intake using the SST model.

lence kinetic energy is large.

6.3 Quantitative Comparisons

In this section, we show the numerical results of 2D simulations using the SST model and consider the effects of "k inclusion", "Re tensor trace" and "diffusion". The turbulence model is used here without considering/modelling the effects of laminar-turbulent transition.

Fig. 13 illustrates the pressure distribution along the upper wall of the intake predicted by the SST model. As expected, the most significant difference appears around the second separation bubble at the entrance of the interior part. Inclusion of turbulence kinetic energy delays the

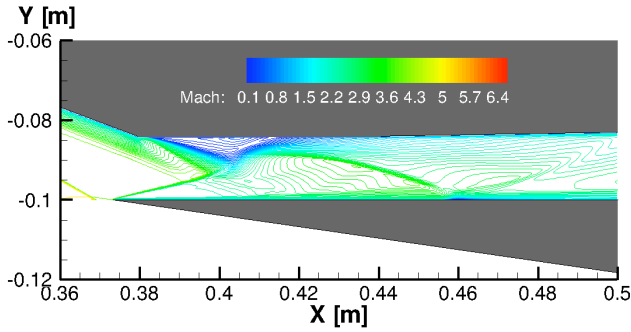


Fig. 11 : Plot of Mach lines at the entrance of the interior part. The turbulence kinetic energy is not included into the total energy . 2D simulation using the SST model.

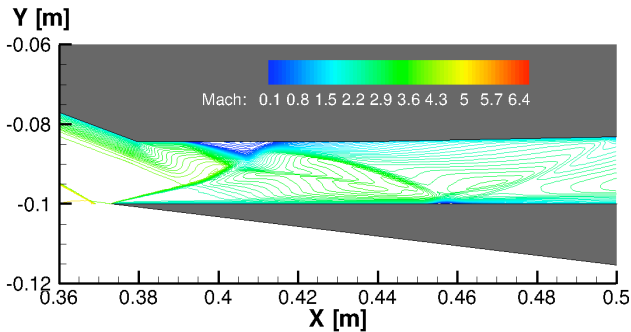


Fig. 12 : Plot of Mach lines at the entrance of the interior part. The turbulence kinetic energy is included into the total energy. 2D simulation using the SST model.

onset of separation and reduces the size of the bubble. This can be seen through the smaller pressure plateau around $x = 0.4\text{m}$. As a consequence of a reduced separation bubble, the reattachment shock wave is stronger and this results in higher pressure peaks downstream of the bubble. In contrast to the obvious effects of "k inclusion", including the turbulent diffusion in the energy equation and the last term on the right hand side in Eqn. 14 do not produce significant difference in the results. This is probably because the magnitudes of these terms are still small in comparison to the other terms in the transport equation.

The heat transfer rate predicted by the SST model is shown in Fig. 14. Here, the differences

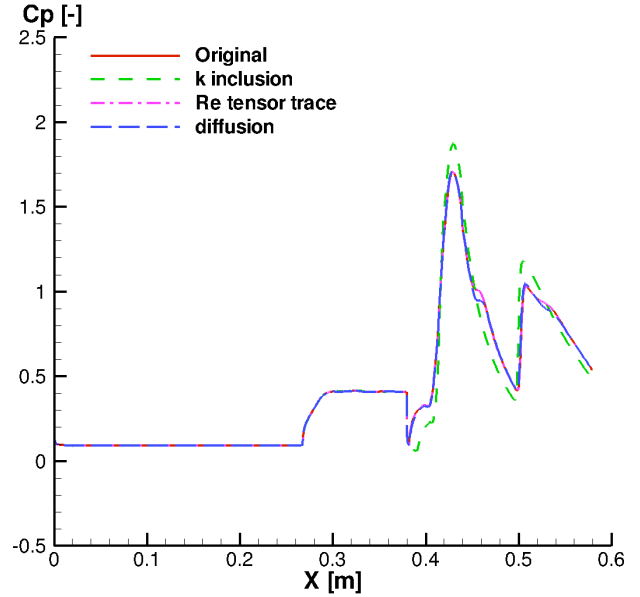


Fig. 13 : Pressure distribution along the upper wall of the intake. 2D simulations using the SST model.

are only due to "k inclusion" and are relatively smaller than in the pressure prediction. This result is also expected because "k inclusion" should have a stronger influence on pressure than on total energy (as discussed in the previous section). Since the effects of "Re tensor trace" and "diffusion" seem to be negligible in this test case, in the next section, we only focus on the computations using "k inclusion".

6.4 The Effects of Compressibility Corrections

Here, we consider the compressibility corrections in combination with the SST transition model and "k inclusion". Fig. 15 and Fig. 16 show the pressure and the Stanton number along the upper wall of the intake. Since laminar-turbulent transition is modeled, the flow on the first ramp is now laminar, therefore the Stanton number is smaller than that in fully turbulent computations. The appearance of a separation bubble between the first ramp and the second ramp around $x = 0.26\text{m}$ is visible through a pressure plateau. This separation did not appear in the fully turbulent

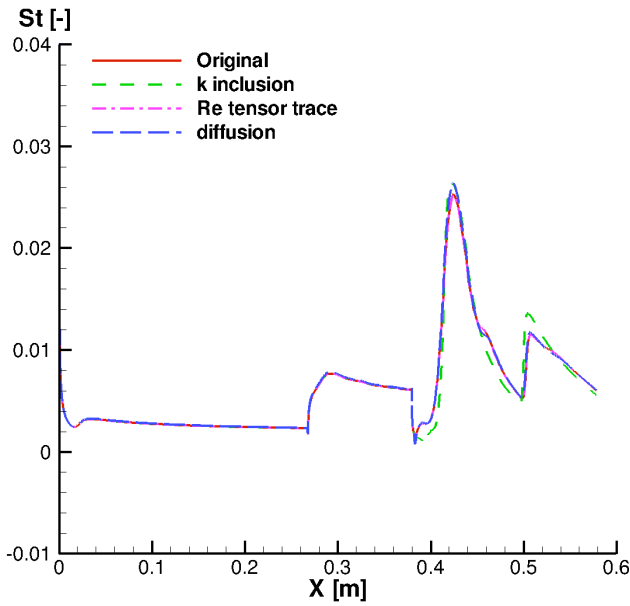


Fig. 14 : Stanton number distribution along the upper wall of the intake. 2D simulations using the SST model.

computations because turbulent boundary layers can sustain higher pressure gradients than laminar boundary layers. Downstream of the second separation bubble, the transition model predicts larger peaks in pressure and Stanton number than the prediction of the fully turbulent computations (see Fig. 13 and Fig. 14).

Regarding the compressibility corrections, two substantial differences can be seen. First, both Wilcox correction and Zeman correction predict larger flow separation at the entrance of the interior part. Second, both corrections reduce the peak of the heat transfer over the second separation bubble. This result indicates that compressibility corrections may change the numerical results significantly and, therefore, are necessary for hypersonic flows.

6.5 Comparisons with Experimental Data

In this section, we present the comparisons of 3D computations with the measurements. The simulations were performed using the SST transition model and the RSM model in which the contribution of turbulence kinetic energy to the total

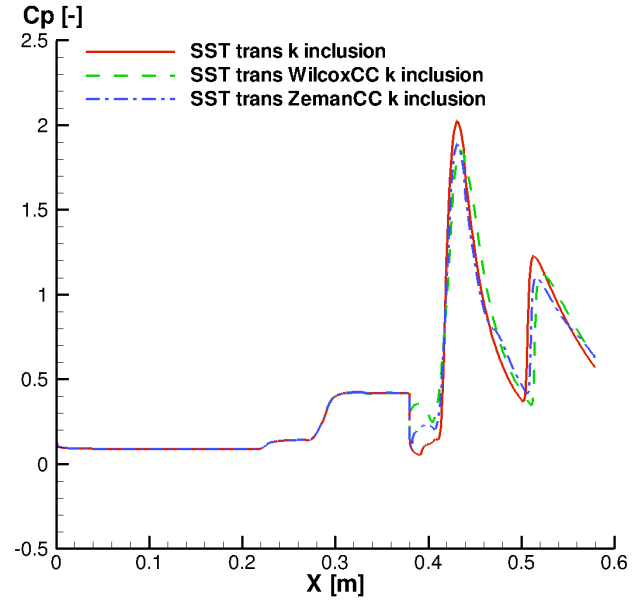


Fig. 15 : Pressure distribution along the upper wall of the intake. 2D simulations using the SST transition model and compressibility corrections.

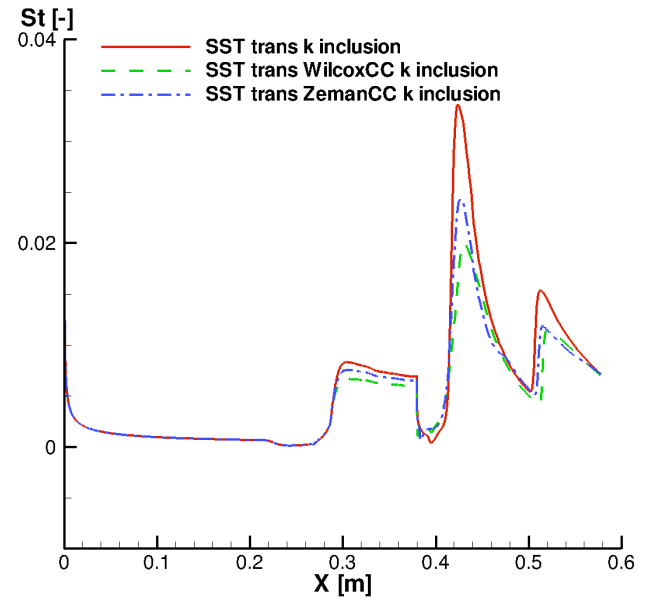


Fig. 16 : Stanton number distribution along the upper wall of the intake. 2D simulations using the SST transition model and compressibility corrections.

energy is included. In the computations using the RSM model, laminar-turbulent transition is taken into account by turning off the turbulence model

for the flow on the first ramp. This method is referred to as "laminar box".

In 3D simulations (Fig. 17 and Fig. 18), the SST transition model does not work in a satisfactory way. The pressure plateau at the entrance of the interior part is significantly lower than the measurements. The Stanton number on the second ramp and the peak of heat transfer rate downstream of the second bubble are also not close to the experimental data.

On the other hand, the prediction of the RSM model follows the measurements closely until after the first pressure peak. The mismatch with the experimental data afterwards is possibly because the reflected shock wave is not predicted accurately. However, it should be noted that the 3D computation of the intake using the RSM model was less stable than the 2D computation and the residual of density leveled off much earlier than in 2D computation. This is probably because the RSM model is more sensitive to the 3D features such as vortices and flow separation which are unsteady in nature.

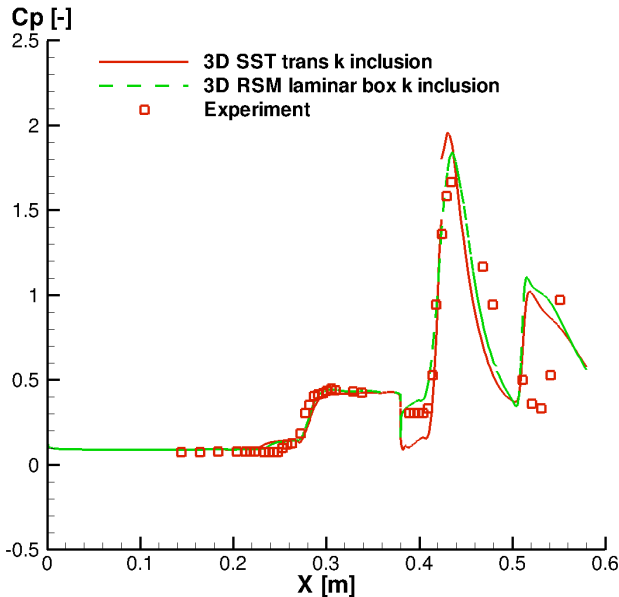


Fig. 17 : Pressure distribution along the upper wall of the intake. 3D simulations using the SST transition model and the RSM model.

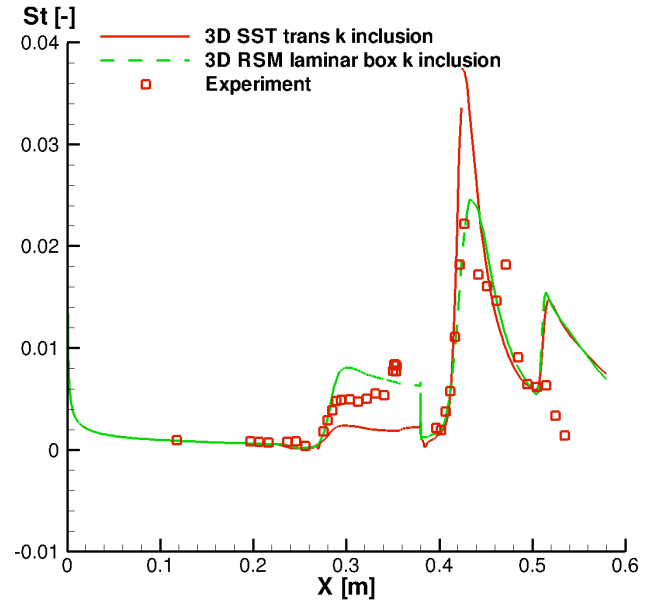


Fig. 18 : Stanton number distribution along the upper wall of the intake. 3D simulations using the SST transition model and the RSM model.

7 Conclusion

We performed a combined study of hypersonic flows in a scramjet intake within the framework of experiment and steady RANS simulation. The experiments were done in a hypersonic shock tunnel. The computations were performed using a finite volume flow solver. Turbulence closure was achieved using two eddy-viscosity models (SST model and SST transition model) and a differential Reynolds-stress model (SSG/LRR- ω model) with several modifications and corrections applicable to compressible flows. Conclusion on the performance and suitability of the turbulence models and the modifications are summarized as follows:

1. The contribution of turbulence kinetic energy to the total energy is necessary and should not be neglected in hypersonic flows with strong shock boundary layer interaction and flow separation. It was shown in this work that turbulence kinetic energy may represent a significant fraction of the total energy and including this quantity may lead to significant differences in the numerical results.

2. Including the turbulent diffusion of k in the mean flow energy equation and including the $2/3\rho k$ in the Boussinesq approximation did not bring any significant differences to the numerical results for this specific test case.

3. Compressibility corrections such as the dilatation dissipation proposed by Zeman and Wilcox [12] may provide significant differences, especially in the heat transfer rate around the separation bubble. Further study is needed to assess the applicability of the compressibility corrections.

Acknowledgements

This work was supported by the German Research Foundation (DFG) within the framework of the GRK 1095 "Aero-Thermodynamic Design of a Scramjet Propulsion System for Future Space Transportation Systems" and the Aachen Institute for Advanced Study in Computational Engineering Science (AICES, RWTH Aachen University). Computing resources were provided by the RWTH Aachen University Center for Computing and Communication and the Forschungszentrum Jülich.

References

- [1] Bosco A, Reinartz B, and Müller S. Computation of hypersonic shock boundary layer interaction on a double wedge using a differential reynolds stress model. *Proc Proceedings of 27th Int. Symposium on Shock Waves (ISSW-27)*, St. Petersburg, Russia, July, 19-24, 2009.
- [2] Bramkamp F. D, Lamby P, and Müller S. An adaptive multiscale finite volume solver for unsteady and steady flow computations. *Journal of Computational Physics*, Vol. 197, pp 460–490, 2004.
- [3] Brodersen O, Ronzheimer A, Ziegler R, Kunert T, Wild J, and Hepperle M. Aerodynamic applications using megacads. *Proc Proc. of 6th International Conference on Numerical Grid Generation in Computational Field Simulations*, pp 793–802. Ed. M. Cross, J. Haeuser, B. K. Soni, J. F. Thompson, ISGG 1998, 1998.
- [4] Eisfeld B. Implementation of reynolds stress models into the dlr-flower code. IB 124-2004/31, DLR, Institute of Aerodynamics and Flow Technology, 2004.
- [5] Fischer C and Olivier H. Experimental investigation of the internal flow field of a scramjet engine. AIAA Paper 2009–7369, September 2009.
- [6] Krause M and Ballmann J. Enhanced design of a scramjet intake using two different rans solvers. *Proc 26th International Symposium on Shock Waves, Goettingen, Germany, 15-20 July 2007*, pp 589–594, 2007.
- [7] Krause M and Behr M. Modeling of transition effects in hypersonic intake flows using a correlation-based intermittency model. *Proc 15th AIAA International Space Planes and Hypersonic Systems and Technologies Conference, Dayton (OH), USA, 28 April - 1 May 2008*.
- [8] Menter F. R. Two-equation eddy-viscosity turbulence models for engineering applications. *AIAA Journal*, Vol. 32, No 8, pp 1598–1605, August 1994.
- [9] Menter F and Langtry R. A correlation-based transition model using local variables part1 - model formulation. *Proceedings of ASME Turbo Expo*, 2004.
- [10] Neuenhahn T and Olivier H. Influence of temperature effects on the shock wave/boundary layer interaction of a scramjet-inlet. *Proc DGLR-Jahrestagung*, Darmstadt, Germany, September, 2008.
- [11] Reece G. J, Launder B. E, and Rodi W. Progress in the development of a reynolds-stress turbulence closure. *Journal of Fluid Mechanics*, Vol. 68, pp 537–566, 1975.
- [12] Rumsey C. L. Compressibility considerations for $k-\omega$ turbulence models in hypersonic boundary layer applications. NASA Technical Memorandum 215705, Arpil 2009.
- [13] Sarkar S, Speziale C. G, and Gatski T. B. Modelling the pressure-strain correlation of turbulence: an invariant dynamical systems approach. *Journal of Fluid Mechanics*, Vol. 227, pp 245–272, 1991.
- [14] Smits A. J and Dussauge J.-P. *Turbulent Shear Layers in Supersonic Flow*, chapter 1. Springer Science + Business Media, Inc, 2006.
- [15] Weigand B, Gaisbauer U, Reinartz B, Kau H.-P, and Schröder W. Das graduiertenkol-

leg 1095/1: Aero-thermodynamische Auslegung eines Scramjet-Antriebssystems für zukünftige Raumtransportsysteme. *Proc Proceedings of Deutscher Luft- und Raumfahrtkongress 2006*, Braunschweig, Germany, November 6-9, 2006. DGLR.

- [16] Wilcox D. C. *Turbulence Modeling for CFD*, chapter 5. DCW Industries, Inc., 1994.

Copyright Statement

The authors confirm that they, and/or their company or organization, hold copyright on all of the original material included in this paper. The authors also confirm that they have obtained permission, from the copyright holder of any third party material included in this paper, to publish it as part of their paper. The authors confirm that they give permission, or have obtained permission from the copyright holder of this paper, for the publication and distribution of this paper as part of the ICAS2010 proceedings or as individual off-prints from the proceedings.